Development of Two-Dimensional Steerable Reflectarray With Liquid Crystal for Reconfigurable Intelligent Surface Applications

Xiaotong Li, *Student Member, IEEE*, Hiroyasu Sato, *Member, IEEE*, Hideo Fujikake, *Senior Member, IEEE*, and Qiang Chen, *Senior Member, IEEE*

***Abstract*— In this article, a reconfigurable reflectarray (RA) system which can steer reflected beam at two dimensions based on liquid crystal (LC) technology at Ka band is proposed. In the RA system, an individually controlled RA unit is come up with and utilized to generate a 12 × 12 elements RA, a novelty bias network composed of metalized vias holes and driving lines are proposed and used to control each element independently, and a Ka band standard horn antenna is offset 20° at H-plane as the primary feed. The manufactured RA model is checked for the reconfigurability with bias voltage under the microscope, then the model is measured that a continuous phas-varying ability can be achieved. During the measurement of beam steering, far-field patterns at E-plane from 0° to 35° are measured; and scanning at H-plane can cover from 0° to 40°; for the special beam direction $\varphi_a = 115°$, $\theta_a = 15°$, a near-field measurement is used and proves that the 2-D beam scanning is possible. Then LC RA is applied as reconfigurable intelligent surface (RIS) in the simulated narrow street model, and the results show that it could indeed enhance the received power of electromagnetic waves. The innovation of this study is to propose a single controllable LC RA unit and a corresponding bias network composed of metallized vias and driving lines; thus, each element in RA can be controlled to change reflection coefficient and beam steering of greater freedom with LC technology is achieved, which is a potential RIS and provides a possible solution for the beam scanning property.**

***Index Terms*— 2-D, beam steering, liquid crystal (LC), reconfigurable intelligent surface (RIS), reflectarray (RA).**

I. Introduction

RECONFIGURABLE intelligent surfaces (RISs) are currently being widely studied [1], [2], [3], [4], [5] as a potential key to open the door of high-frequency wireless communications owing to their unique configurabilities such as controlled-direction beam, multibeam, and beam forming, such a steering property of beam can be used in programmable transmitters or receivers to further strengthen the signal to the end users in need and guide the electromagnetic wave transmitting to the desired districts. As a promising bridge, RIS can significantly lower the extreme requirements of wireless transmitters while avoiding the high costs of employing a large number of micro-cells in unit area. Nowadays, various means [6], [7], [8], [9] are being tried to achieve reconfigurabilities in RIS. Among them, reconfigurable reflectarray (RA) [9], [10], [11], [12] is the most popular one due to its unique properties: low loss due to the absence of a corporate feed, ease of fabrication, planarity, and low weight and lower cost.

In the research of reconfigurable RA, the reconfiguration is realized by various means, mainly including programmable lumped devices, mechanical devices, and tunable materials. RA element based on lumped devices have been widely studied [13], [14], [15]. By controlling elements such as p-i-n diodes and varactor diodes with different circuits, the lumped devices can be used as switch. Although practical, these lumped elements cannot be used as ideal switch in millimeter wave regime, owing to the intrinsic parasitic effects. Mechanical approaches [16], [17], [18] use mechanical systems like MEMS to physically modify the structure sizes which are sensitive to EM response. While mechanical mechanisms can provide high accuracy, the cost increases since EM devices at high-frequency bands require high accuracy, and mechanical approaches are relatively slow compared to electrically controlled methods. As a tunable material, liquid crystal (LC) can be integrated to the RA by treating it as a permittivity-changeable media [19], which can respond to voltage quickly [20] and cost is low.

The first LC RA is proposed in [21] and beam scanning is achieved by the LC RA with three-dipole structure [22], it can just steer beam at the E-plane, similar works are found in [23] and [24]. The same unit design employing the idea of subarray [25], a group of elements can be controlled differently both in line and rows, thus beam scanning at two dimensions can be achieved. By controlling the effective length in the unit, some scholars achieved controlling the 2-D phase varying and beam scanning [26] with four-layer structure. In this study, a novel and simpler LC RA unit has been designed with only three layers, featuring a unique bias circuit with metallized perforated vias and driving lines. This design allows for a larger range of phase variation while also scaling down the fabrication cost, although it comes at the expense of a certain reduction in reflected wave magnitude. However, the advantages of this LC RA design are significant. The designed LC RA unit achieves independently controllable elements, allowing for precise control of the

Manuscript received 28 February 2023; revised 27 November 2023; accepted 29 December 2023. Date of publication 22 January 2024; date of current version 7 March 2024. This work was supported by the Ministry of Internal Affairs and Communications in Japan under Grant JPJ000254. *(Corresponding author: Xiaotong Li.)*

Xiaotong Li, Hiroyasu Sato, and Qiang Chen are with the Department of Communications Engineering, Tohoku University, Sendai 980-8579, Japan (e-mail: li.xiaotong.r4@dc.tohoku.ac.jp).

Hideo Fujikake is with the Department of Electronic Engineering, Tohoku University, Sendai 980-8579, Japan.

Color versions of one or more figures in this article are available at https://doi.org/10.1109/TAP.2024.3354054.

Digital Object Identifier 10.1109/TAP.2024.3354054

phase of the reflected waves. Moreover, this LC RA enables 2-D beam scanning, where the scanning direction is not just limited to the E-plane and H-plane, providing greater beam scanning freedom and flexibility. By utilizing this novel LC RA design, the study successfully addresses the limitations faced by conventional LC RA designs, such as limited phase shifting range and fixed scanning directions. This advancement offers promising potential for various applications in wireless communication and beam forming systems, with the added benefit of cost-effectiveness in fabrication. In the realm of high-frequency antennas, approaches based on reflection characteristics have garnered increasing attention in recent years. Notable examples include the utilization of cardiac pulse for detection [34] and the application of reconfigurable RAs in RIS setups to achieve blindness trapping [6], [35]. While diode-based RAs have been previously employed for RIS [6], [35], our study introduces a novel concept by introducing LC RA as RIS. This innovation represents a significant step forward as it addresses and improves upon the issue of quantization lobes associated with low-bit RAs. Different from previous studies focus on increasing the receiving power in the path-loss model [35], [40], we present a solution to eliminate the blind zones of electromagnetic wave in a simulated congested urban experimental scenario by RIS incorporating LC RA as the receiving power from RIS in practical communication environment is more complicated.

Expanding the previous studies on beam scanning at both E-plane and H-plane [27], this work upgrades unit cell structure based on LC technology and considering a biasing circuit and mechanical spacers for realistic full-wave results. These improvements are in view of our plan to prototyping the system not just now, but also in the future works. Therefore, as many engineering problems and details as possible to obtain more accurate predictions of what would happen are considered. To improve the reliability and accuracy of scanning beam, the polarization response of full-wave simulation-derived unit cell, which consists of potentially impactful effects from material losses, coupling effects, possible surface wave, and edge taper. In addition, the incident wave from the feed antenna to the RA surface is calculated by method of moments (MoM), which could give more accurate information of field with co-polarization and cross-polarization compared with approximate cosin q pattern. Based on these careful considerations, we design a LC RA system with feed antenna, LC RA, bias network, and voltage controller [shown in Fig. 1(a)]. And the proposed LC RA system exhibits great potential to serve as a RIS, as shown in Fig. 1(b), the future wireless communication system is forced to move to high-frequency bands (e.g., mm wave) due to the tightening of spectrum resources, but the mm wave is hard to penetrate the building, and the path loss is large, which is prone to cause the end user to receive weak signals. If the LC RA is assembled on the surface of the building, the beam can be controlled to point of the blind zone of the base station by adjusting the unit of the LC RA, so as to improve the problem of communication.

This article is organized as follows: Section I introduces the development of LC RA, talks about the advantages and disadvantages of previous studies on LC RA. Section II introduces the single controllable LC RA unit, explains the working principles, describes the details of the unit, andthen shows the simulation results of the LC RA unit at the periodic structure in commercial software HFSS. Section III presents the manufactured LC RA model and shows the innovated bias network connecting to the element, then measures the steered phase of LC RA with bias voltage. Section IV exhibits the measured steered beams and proves the beam steering properties at two dimensions. Section V shows an experiment which is valuable for RIS in actual application scene. Section VI concludes this article.

II. Design Individually Controllable LC RA Unit

A. Developed LC RA Unit

Based on the RA unit of two-finger structure [see Fig. 2(a)], we have developed a new LC RA unit shown in Fig. 2(b); a slot along the direction x is added at the ground. Thus, the ground of the LC RA is separated into square metallic ground, which can be biased with the needed voltage relative to the patch layer. The small square-shaped ground on FR4 replaces the original discrete ground on quartz glass; to control the state of LC, a metalized vias through FR4 connects to the electrode on other side of FR4. In the former LC RA [see Fig. 2(c)], the reflection phase can just be controlled along one direction; with the updated unit, each unit in the LC RA can be biased with the voltage to compensate the incident wave, thus beam scanning in 2-D is achieved.

The LC RA element with multilayer structure is shown in Fig. 3; different from the former 2-fringer structure, a slot on the bottom metal layer of glass is attached to separate the ground in the direction y which is orthogonal to the path layer. The 3-D view model is presented in Fig. 3(a) and the top view of RA unit is presented in Fig. 3(b). The schematic of controlled states of RA are compared in Fig. 3(c) and (d), the LC molecules inside the LC RA are along direction x after the prearrange, the relative permittivity of LC is $\varepsilon_{r,\perp}$; the LC molecules will rotate along direction z with bias voltage increases, the maximum value of relative permittivity for LC is $\varepsilon_{r,//}$. The detailed information of each layer is exhibited in Fig. 3(e). The top of the RA unit is quartz glass which has good electromagnetic properties ($\varepsilon_r = 3.78$, $\tan\delta = 0.002$) and strong rigidity, the patch layer of metalized 2-finger structure is coated under the quartz glass. The third layer and the fifth layer are polymide which is used to guarantee the initial state of LC molecules. LC is sealed at the fourth layer by solid media with the polymide coated on the surface. The six layer is the square metalized sheet to add bias voltage relative to the patch layer. The bottom layer is FR4 board with metalized vias through the board and the metalized vias is added to connect voltage. The parameters of the LC RA unit are marked in Fig. 3. The same model is simulated in software HFSS. By choosing the same material properties of 5 μm-thick-golden for metalized layer next to LC, the vias and bias point is set silver, and the values of the parameters with wavelength at target frequency 37.5 GHz are listed in Table I.

The parameters listed in Table I exert varying effects on the reconfiguration performance of the LC RA. Here is a

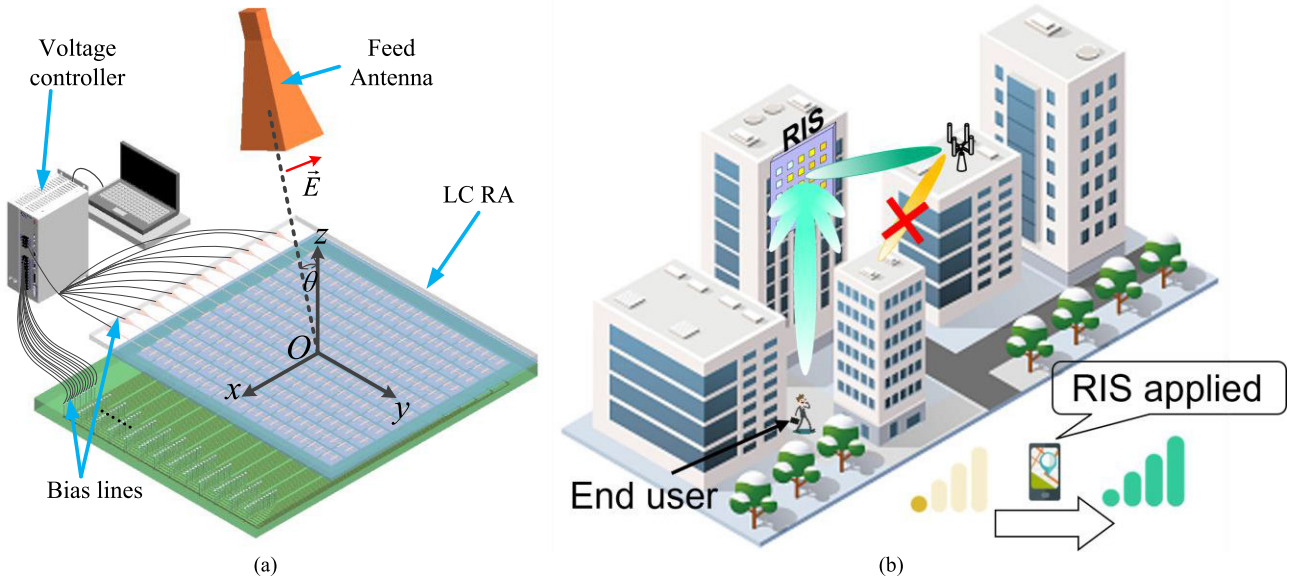

Fig. 1. Schematic of applying LC RA as RIS. (a) LC RA system consists of primary feed horn antenna, LC RA, bias network, bias lines, voltage controller, and computer. (b) Application of RIS to increase the receiving signal power in future crowded areas.

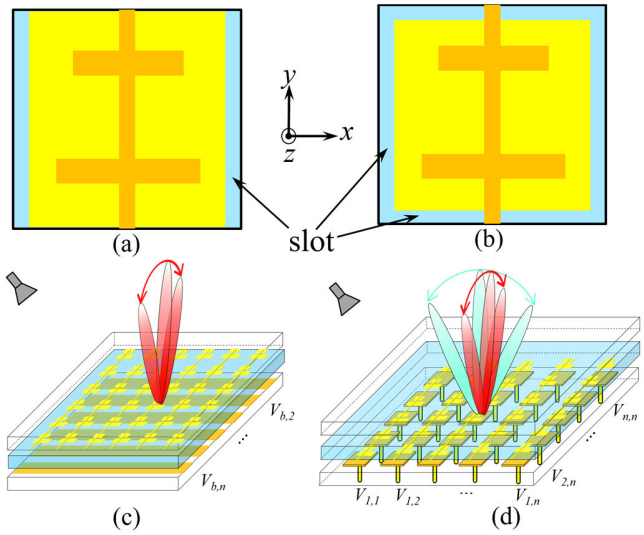

Fig. 2. Updated LC RA to achieve beam scanning in two dimensions. (a) Original LC RA unit. (b) Individual controllable LC RA unit achieved by adding slots at the bottom of ground. (c) Beam scanning at 1-D achieved by bias scheme along one direction. (d) Beam scanning at 2-D achieved by individual controllable LC RA unit and corresponding bias voltage at 2-D.

TABLE I
UNITS PARAMETERS

Variable	Numerical Values/ mm	Variable	Numerical Values/ mm
h_G	0.60 (0.075λ_0)	h_{GB}	1.20 (0.15λ_0)
X	4.00 (0.5λ_0)	h_{LC}	0.20 (0.025λ_0)
G	3.90 (0.4875λ_0)	Gap	2.00 (0.25λ_0)
L_{x1}	1.95 (0.244λ_0)	W	0.30 (0.0375λ_0)
L_{x2}	2.10 (0.2625λ_0)	W_0	0.20 (0.025λ_0)
R	0.50 (0.0625λ_0)	R_b	0.70 (0.0875λ_0)

breakdown of how these parameters influence the LC RAs behavior. Glass thickness (h_G): the thickness of the glass affects the equivalent port impedance of the LC RA, leading to periodic variations in the reflection coefficient magnitude with frequency. However, it does not significantly impact the phase shift range. Unit period (x): the period of the LC RA, x, is often set equal to or less than $\lambda_0/2$ to minimize sidelobe level (SLL) when scanning the beam. Ground length (G): the size of the square metallic ground is usually chosen to be similar to X to prevent leakage of the incident wave. When G approaches the size of the patch, the reflection coefficient magnitude becomes smaller, and phase shift may be negligible. Finger lengths (L_{x1} and L_{x2}): L_{x1} and L_{x2} determine the resonant frequency of the LC RA, increasing their lengths typically leads to a decrease in the resonant frequency. Metal finger width (W): W affects the current distribution, increasing W can lower the resonant frequency to some extent. Driving linewidth (W_0): the width of the driving line should be kept thin to avoid interfering with the current distribution along the x-direction on the patches. Dielectric thickness (h_{GB}): the thickness of the FR4 board, a thicker h_{GB} is chosen to prevent deformation during processing, as electromagnetic waves reflect from the metal layer above. Thickness of LC layer (h_{LC}): increasing h_{LC} enhances the reflection magnitude but simultaneously reduces the phase shift range. Distance between metallic finger (Gap): a small Gap value increases the mutual inductance of the patches, causing a decrease in the reflection magnitude and compression of the phase shift range, a Gap of $\lambda_0/4$ is often considered suitable. Connection parameters (R and R_b): R and R_b mainly serve as connectors between the vias and driving lines, and do not have a significant impact on the reflection magnitude or phase shift. Considering these effects helps in optimizing the design and performance of the LC RA.

In this work, all the parameters in Table I tried to sweep and optimize the parameters of this structure to achieve larger phase shift range over 300° and relative high reflection coefficient, which are two basic principles for RA element design. The type of LC used in this study is TD-1020XX with mixture; its material parameters at Ka band are measured as: relative permittivity changes from $\varepsilon_{r,\perp} = 2.4$ to $\varepsilon_{r,//} = 3.2$, loss tangent varies from $\tan\delta_\perp = 0.014$ to $\tan\delta_{//} = 0.004$, and the

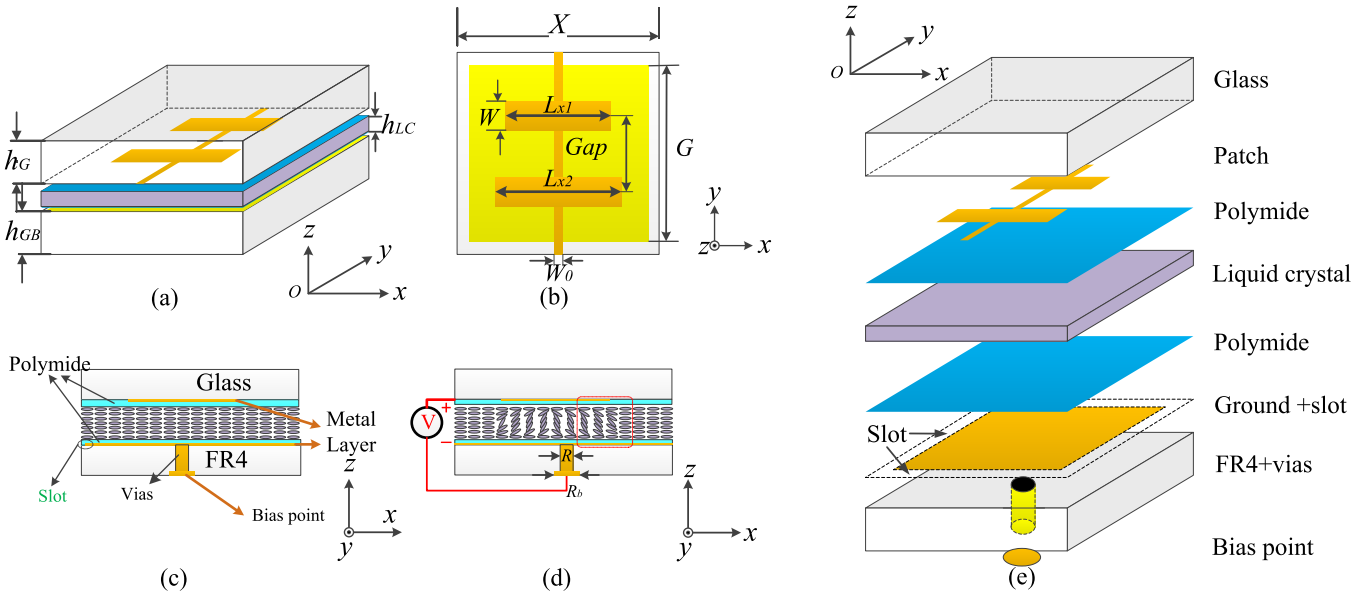

Fig. 3. Structure of LC RA unit. (a) 3-D view of LC RA unit. (b) Top view of LC RA unit. (c) Side view of LC RA unit when the LC is not biased. (d) Side view of LC RA unit when the LC is biased. (e) Detailed description of LC RA layers.

relationship of relative permittivity increase with bias voltage increasing with a quasi-linear curve has tested in [28] and [29]. Even though the distribution of $\varepsilon_{r,\mathrm{LC}}$ at different part of LC RA unit is inhomogeneous according to the structure of electrodes, simulating the LC partition with different values may be more realistic [37], simulation and experiments in former studies showed that the simulation of LC with inhomogeneous LC and homogeneous LC are almost the same [38], and simulating LC with homogeneous $\varepsilon_{r,\mathrm{LC}}$ value is acceptable for studying the variation properties of LC and prediction for beam steering. So electrically controlled reconfiguration can be applied by adding voltages to change the dielectric constant and loss tangent of LC in each unit cell, and the permittivity of the LC has strong relationship with voltage [30]. If the RA unit has different performance of reflected wave when dielectric constant is steered, which means the proposed LC RA unit can be steered by electivity.

B. Performance of LC RA

The performance of the LC RA unit under normal incidence is simulated in commercial software with the infinite periodic structure approximation based on Floquet theory. The LC RA unit model of Fig. 3 is simulated in HFSS with the LCs initial state ($\varepsilon_{r,\perp} = 2.4$, $\tan\delta_\perp = 0.014$). The relationship between the reflected wave and the incident wave can be characterized by reflection coefficient considering the polarization influence. The reflection coefficients at the interested frequency band from 33.0 to 43.0 GHz are shown blew; in the scattering matrix, the first alphabet of the subscript denotes the polarization of reflected fields, along with the second alphabet of the incident fields

$$\begin{bmatrix} E_{r,x} \\ E_{r,y} \end{bmatrix} = \bar{\bar{\Gamma}} \begin{bmatrix} E_{i,x} \\ E_{i,y} \end{bmatrix} \tag{1}$$

$$\bar{\bar{\Gamma}} = \begin{bmatrix} \Gamma_{xx} & \Gamma_{xy} \\ \Gamma_{yx} & \Gamma_{yy} \end{bmatrix}. \tag{2}$$

Fig. 4 presents the simulated reflection response comparison between the LC RA with slots and without slots. The simulation results depict Γ_{xx}, which corresponds to the cell's co-polarization along the x-direction, within the frequency range of 33.0–43.0 GHz. Comparing the LC RA with the cell that lacks a slot, the introduction of a slot leads to several notable changes. Resonant frequency: the resonant frequency of the LC RA is increased by the inclusion of the slot, shifting from 39.3 to 40.6 GHz. Reflection magnitude: with the addition of a slot, the reflection magnitude diminishes. Specifically, the minimum reflection magnitude decreases from −4.4 to −5.7 dB. Phase shift: the introduction of a slot just shifts the resonant frequency while phase still varies from −600° to 100°, and reflection phase decrease with frequency increase. The phase variation range and trend remain consistent despite these shifts. In summary, the addition of slots to the LC RA increases its resonant frequency shift upward and decreases the reflection magnitude, but the overall phase variation range and tendency of the LC RA cell keeps still; they are not greatly affected by the addition of slots.

In this study, the LC TD-1020XX is used for manufacturing LC RA. Prior to the LC RA design, we conducted comprehensive tests to assess the reconfigurability of the LC TD-1020XX within Ka band. The results of our tests revealed that the equivalent relative permittivity of the LC ranged from 2.4 to 3.2, corresponding to bias voltage variations from 0 to 36 V. Moreover, the equivalent loss tangent of LC demonstrated a notable decrease, ranging from 0.014 down to 0.004, as the voltage was increased. This empirical data play a crucial role in guiding the design and optimization of our LC RA system. Thus, the change $\varepsilon_{r,\mathrm{LC}}$ from 2.4 to 3.2 is accompanied by a variation in $\tan\delta_{\mathrm{LC}}$ from 0.014 to 0.004 in the simulation model at frequency band from 33.0 to 43.0 GHz to mimic the bias condition. The frequency response of the reflection coefficients (Γ_{xx}) for different values of equivalent relative permittivity in the LC layer is shown in Fig. 5. The

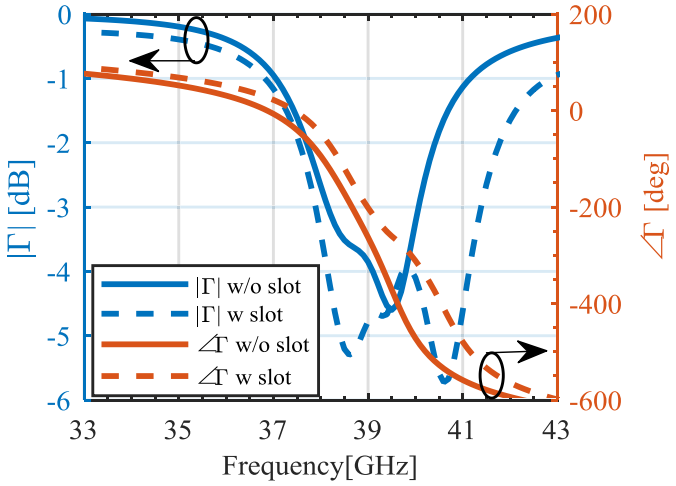

Fig. 4. Comparison of simulated reflection coefficient of the LC RA unit with and without slot on the ground.

magnitude of the reflection coefficient of RA is shown in Fig. 5(a), when the LC RA is not biased, the magnitude of reflection coefficient changes from −0.2 to −5.9 dB at the band from 33.0 to 43.0 GHz; when the unit is biased, the relative permittivity increasing and loss tangent decreasing, the reflection coefficient magnitude varies from −0.3 to −8.9 dB. The phase of the reflection coefficient from RA is shown in Fig. 5(b), and the phase variation scale of more than 330° is achieved in the structure at the frequency band from 37.4 to 39.7 GHz when relative permittivity changes. From the results of frequency response vias reflection coefficient when LC presents different values of relative permittivity, it can be tried to compensate phase continuously, and this property can be applied to steer beam.

Incident angle is also an important factor for the RA. When the feed antenna is located somewhere near the RA, the incident wave always has angle differences with different elements distributed on the RA aperture. The reflection coefficient (Γ_{xx}) response with relative permittivity of LC is simulated when incident wave changes incident angles from 0° to 45° at target frequency $f = 37.5$ GHz, results of Γ_{xx} from incident angles 0°, 15°, 30°, and 45° are shown in Fig. 6(a). From the figure, the magnitude variation appears when incident angles relative to normal direction increase. When incident angle increases, the magnitudes of Γ_{xx} at different state of LC varies a lot; at the initial state ($\varepsilon_{r,\perp} = 2.4$) and final state ($\varepsilon_{r,//} = 3.2$) of LC, the magnitude varies little, and at the middle state ($\varepsilon_r = 2.7$), $|\Gamma_{xx}|$ at 45° decrease 2.1 dB compared with normal incident condition. The reflection coefficient phase with relative permittivity of LC varies little compared with magnitude. The phase difference has a maximum difference of 24° when there is a change in the incident angle, just 6.9% deviations in the critical phase performance. The electrical field distribution of three cross sections and electrical current distribution on the metallic layer at $f = 37.5$ GHz are plot in Fig. 6(b) when the LC is not biased. The same distributions are plot in Fig. 6(c) when LC is biased to the maximum value of $\varepsilon_{r,\mathrm{LC}}$. With the relative permittivity changing, the currents distribution on the patch structure and RF field at three sections (L_{x1}, L_{x2}, and D) around the metal shows that when the relative permittivity of LC increases, the resonant states of two dipoles shift to one dipole (the longer one).

III. LC RA Model

A. Bias Network

From investigation of LC RA, static driving-line bias network is a type of highly integrated and stable method to control beam scanning. The previous works of reconfigurable LC RA are mostly focused on 1-D RA, because the electrodes only connect the patch element of a row or a column to add the voltage of the same value in this linear group [22], [30]. But the driving-line bias network ends up in problem when 2-D reconfigurable RA is controlled, because when the driving line is connected to the patch layer to achieve the reflection coefficient of each element in the 2-D RA, the driving-line will pass through the gaps between patch layers of elements in both the x and y directions, which is obviously destructive for the reflected waves of the RA. However, the 2-D beam scanning of reconfigurable RA requires the phase of each element to be independently steered, resulting in the fact that uniform biased voltage within one driving line is no longer sufficient.

To erase the influence of driving lines on electromagnetic properties of RA, a bias network composed of 2-D driving line and the metalized vias is utilized in the controlling module. The LC RA with bias network is sketched in Fig. 7. As can be seen in Fig. 7(a), the 2-D LC RA has three parts: quartz glass with metallic 2-finger structure at the bottom, LC layer, and ground layer with bias network. As the superstrate of LC RA, the quartz glass has an advantage of low loss and strong stiffness; underneath the quartz glass is the metallic two-finger structure patch layer pointing in the x-direction, the two-finger structures are connected to the drive line along the y direction with a period of 4.0 mm, and there is a dc pad at the end of the drive line. The ground layer is shown in Fig. 7(b); at the upper part [see Fig. 7(c)], the square metallic layers are discretized by slots in xy plane and connected to driving lines [see Fig. 7(d)] at the back of the FR4 board through metalized vias. The driving lines at the same row along direction x has the same length shift along x and driving lines in one column have different length shift along y, then the driving lines are bent to extend to the $+x$-direction.

The proposed bias network is a crucial component that empowers each individual cell of the LC RA with the capability of independent bias voltage control. This control mechanism is employed to compensate for the reflection phase of the LC RA, thereby enabling beam scanning in two dimensions. The operational scheme of this network can be described as follows: to establish a baseline, a reference voltage is applied to the patch layer of the LC RA unit. For each specific LC RA unit, a desired voltage difference is introduced to the driving lines. This voltage difference is determined in relation to the reference voltage at the patch layer. The voltage difference from the driving lines is transmitted toward related square grounds [shown in Fig. 7(c)] at the bias point [see Fig. 7(b)]. The voltage difference is further conveyed to the square ground sections through the solid metallic vias,

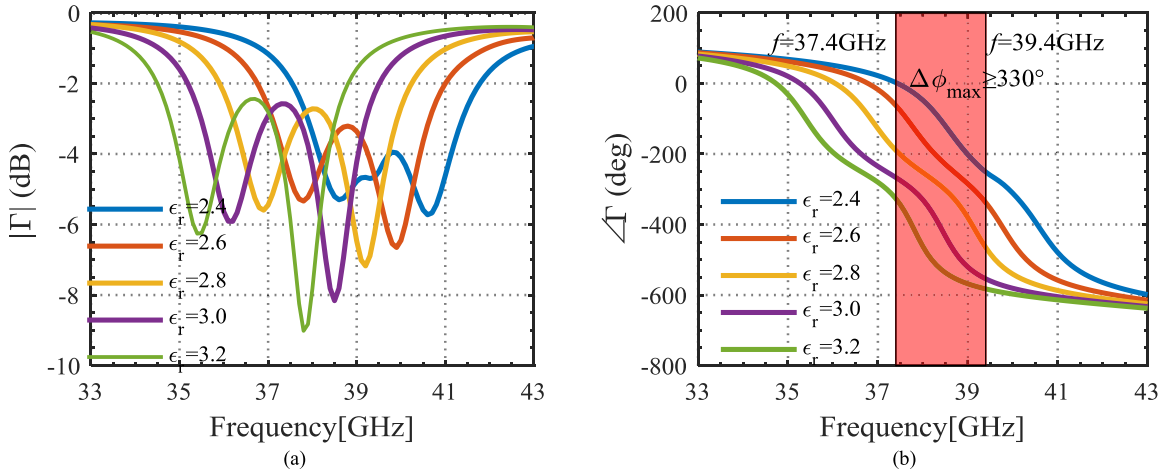

Fig. 5. Frequency response of the reflection coefficient for different values of equivalent relative permittivity in the LC layer. Frequency response of reflection coefficient (a) magnitudes and (b) phases when LC presents different values of relative permittivity.

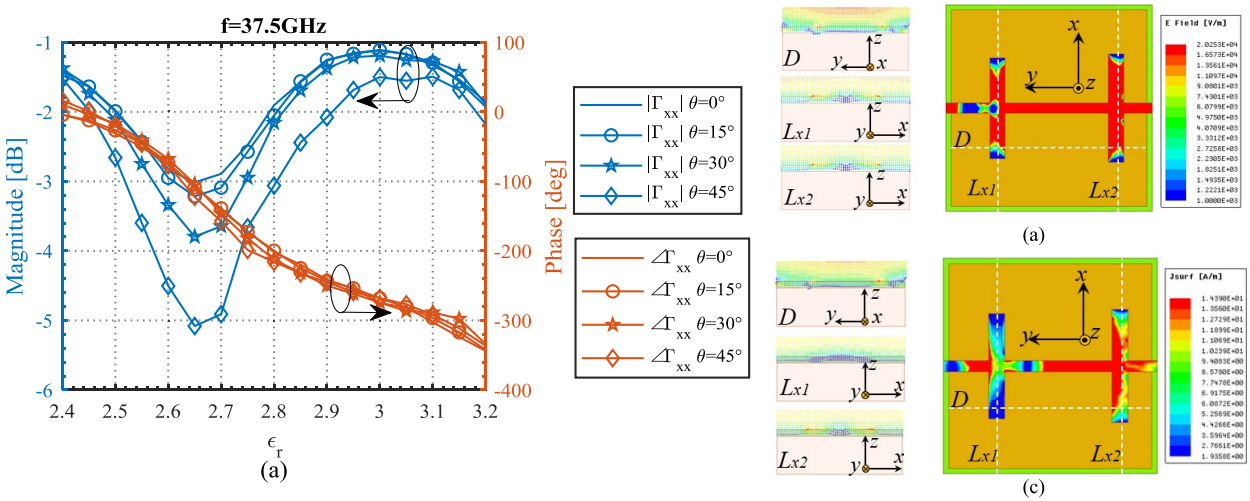

Fig. 6. Reconfigurability at f = 37.5 GHz. (a) Reflection coefficient response with relative permittivity of the LC when incident wave comes with different incident angles. Electrical density distribution on the path layer and field distribution at the section marked when LC is (b) not biased and (c) fully biased.

as presented in Fig. 7(b). By implementing this comprehensive bias network setup, the LC RA units attain phase-independent controllability. This approach offers greater flexibility and accuracy in controlling the direction of the reflected beams, enhancing the overall performance and capabilities of the LC RA system.

B. LC RA Model Manufacture and Reconfigurability

The fabrication procedures of LC RA are as follows: Step 1—Cleaning Procedures: The surface of glass and FR4 board with ultra-sound cleaning machine with special liquid and pure water for a certain time, then air gun was used to dry the glass. Step 2—Rubbing Process: Polyimide AL1254 was used as alignment film to cover the metal-side surface of glass and FR4. After complicated heating procedures, a rubbing procedure along x-direction is done which allows the LC layer to change in x-direction, then put glass on the rubbing machine to use high pressure to rotate in x-direction of the glass to finish the rubbing. Step 3—Integration Process: Put a small spacer to support the glass with thickness of h_{LC} on the FR4, then put the upper glass with a 7 mm shift at y direction on the FR4 board. After the procedure of inserting LC LIXON-TD1020-XX ($\varepsilon_{r,\perp} = 2.4$, $\tan\delta_\perp = 0.014$, $\varepsilon_{r,\parallel} = 3.2$, $\tan\delta_\parallel =$ 0.004, viscosity at 20 °C is 22.5 mPas), glue is used to seal the edge of glass. The front and back sides of the fabricated model, a 12 × 12 element LC RA with a size of 50.0 × 50.0 mm, are shown in Fig. 8(a) and (b), bias lines are connected to the backside by pins, and the patch layer is also connected to bias lines.

Since the permittivity change, the refractive index will also change, thus the observed reflected visual light can be observed differently. This phenomenon can be used to check the reconfigurability of the LC RA. The LC RA element is checked under microscope to observe the reflected light when LC is biased with different voltage. This experiment is shown in Fig. 8(c). LC RA is placed under the objective lens and the enlarged unit image is projected on the monitor. Tune the diaphragm to observe the intensity of the light, so that the light of the images of the LC RA at two extreme states is observed. Fig. 8(d) is the image of the unit when LC RA is without bias, Fig. 8(e) is the image of the unit when LC RA is biased with the maximum voltage 36.0 V, and the LC under the finger structure has changed the relative permittivity under bias voltage. Even though the material properties at optic band and RF band are different, but they have the same tendency but difference in value.

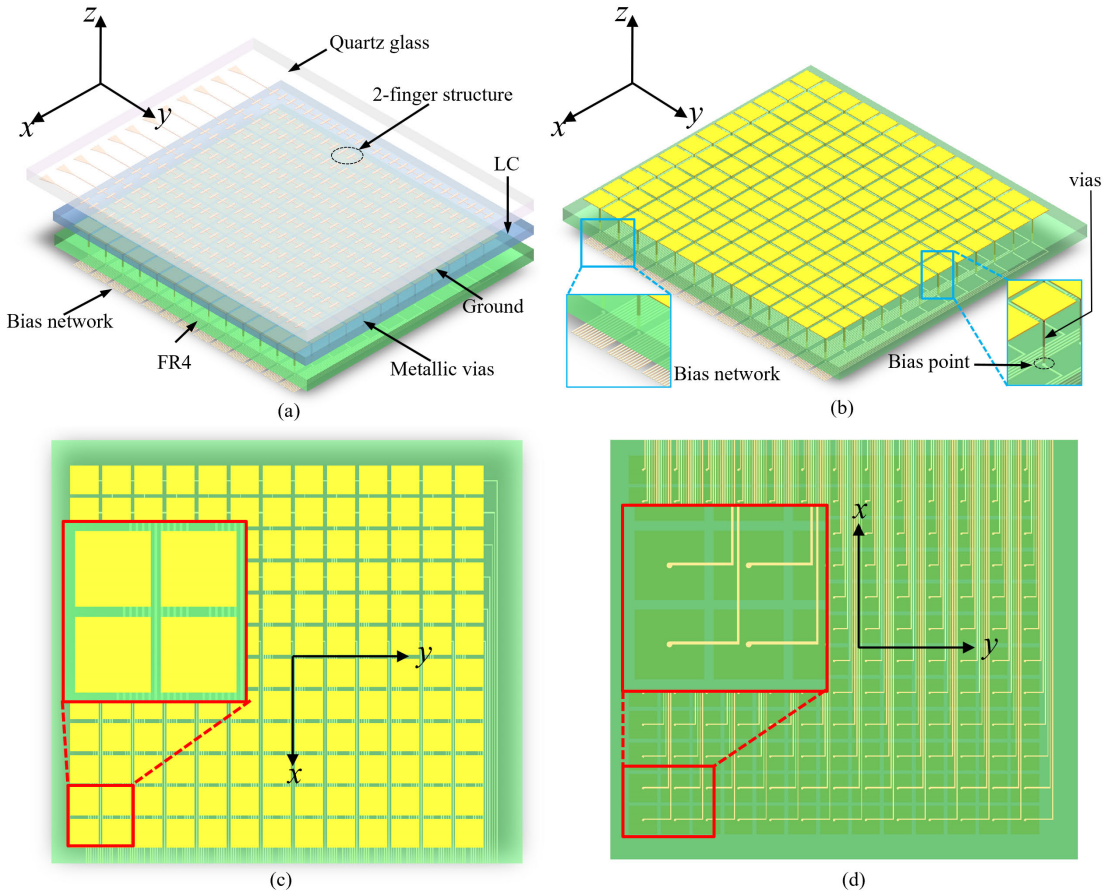

Fig. 7. LC RA with bias network. (a) Whole structure of LC RA. (b) 3-D view of the ground layer with bias network. (c) Top view of the ground layer, the top is discrete rectangle ground. (d) Bottom view of the ground layer, the ground side is the metalized vias connected to driving lines.

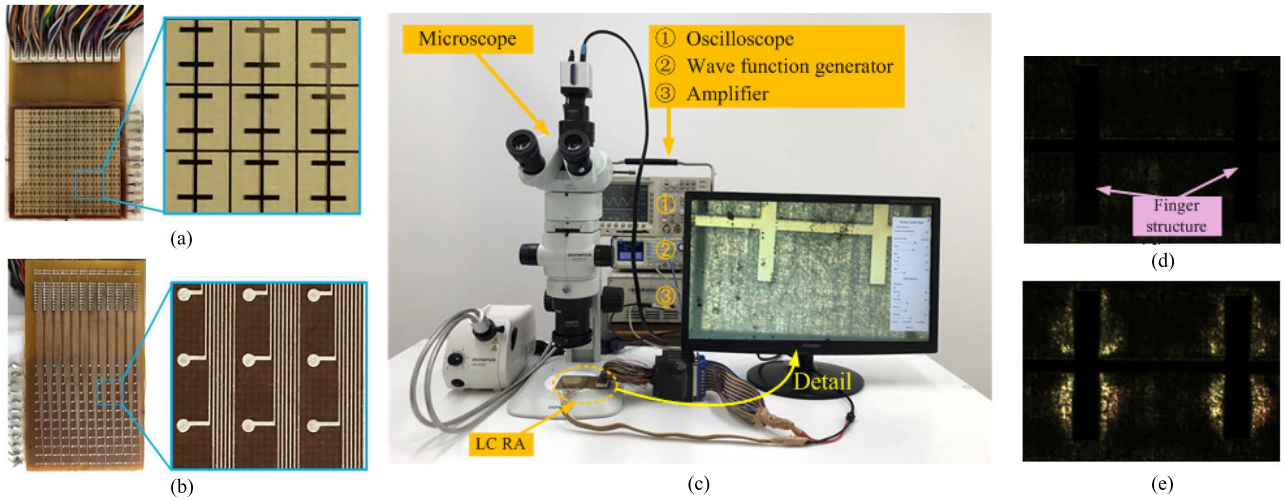

Fig. 8. Manufactured LC RA model. (a) Front image of the LC RA and its detail. (b) Back side image of the LC RA and its detail. (c) Observe the detail of the LC RA with bias voltage under microscope and check its reconfigurability. (d) Unit cell when the RA is not biased. (e) Unit cell when the RA is biased with maximum voltage 36 V.

C. Steering Phase of Reflection Coefficient

To control the reflected wave of LC RA, a steering system is designed: a Labview program is coded on the PC, which can control the wave function generator to output voltage signal with different amplitudes and frequency. Using an amplifier, enough voltages are attained. The output voltages from the amplifier are biased to bias channels of LC RA. In this way, LC can be controlled accurately; at the same time, the scattered field is measured by the lens antenna and is analyzed by Agilent PNA N5224A.

To measure the phase varying ability of LC RA, the experiment setup shown in Fig. 9(a) was used. A lens antenna which can generate focused plane wave is placed in front of the LC RA, with E-plane parallel to the direction of dipole structure of LC RA and the distance from the surface of

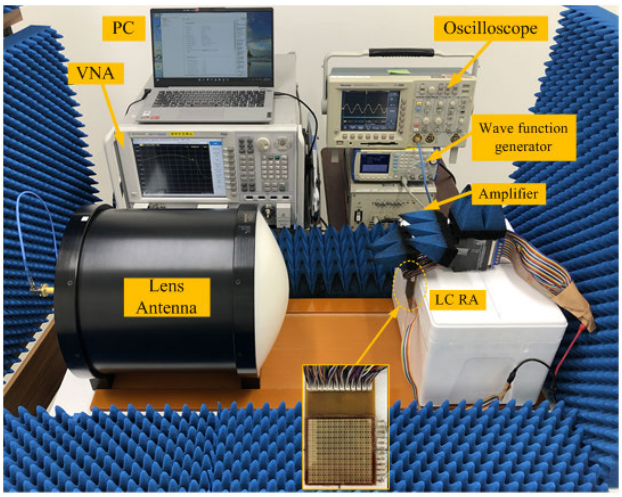

(a)

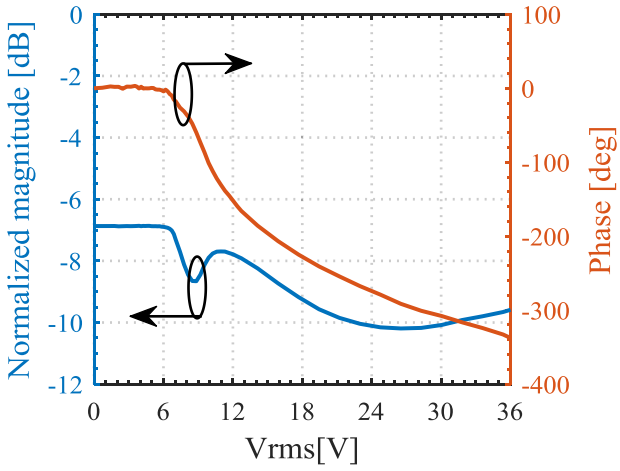

(b)

Fig. 9. Measure the reflection coefficient of LC RA. (a) Actual experiment. (b) Magnitude and phase of reflection coefficient from LC RA.

lens antenna to the LC RA is $F = 300$ mm. The LC RA is placed on the platform made of plastic foam behind which are radio-absorbing materials and all electrodes connected to the patch layer are connected to all the bias lines; thus, all the elements are biased with the same voltage, and scattering field is measured at the broadside of LC RA.

To get the scattered field, inverse Fourier transform ($\mathcal{F}^{-1}$) is applied to the measured frequency domain $S_{11}(\omega)$ to obtain time domain $S_{11}(t)$. A gate function $g_\tau(t)$ is multiplied to $S_{11}(t)$ so scattered field in time domain is obtained; here $r = F = 300$ mm, through Fourier transform ($\mathcal{F}$) to frequency domain, the scattering field can be attained and the details are expressed by the following equations:

$$\vec{E}|_{scat} = \vec{E}|_{total} - \vec{E}|_{inc} \tag{3}$$

$$S_{11}|_{scat} = S_{11}|_{total} - S_{11}|_{inc} \tag{4}$$

$$S_{11}(t) = \mathcal{F}^{-1}[S_{11}(\omega)] \tag{5}$$

$$S_{11}|_{scat}(\omega) = \mathcal{F}\left[S_{11}(t)g_\tau\left(t - \frac{c_0}{r}\right)\right] \tag{6}$$

$$S_{11}|_V = S_{11}|_{scat}(\omega)e^{jkr}. \tag{7}$$

As the receiving power decays with increasing distance between the scatter and Rx antenna, phase also changes at the same time; therefore, a reference is needed to calibrate the reflection coefficient. To the magnitude of reflected wave, it can be referenced to a copper plate with the same size of LC RA. For the phase of the reflected wave, a reference phase of LC RA without bias $\phi|_{0V} = 0°$ is selected. When different voltage value is biased to the LC RA, the controlled reflection coefficient can be observed by the following equations:

$$|\Gamma||_V = [S_{11,scat}|_V / S_{11,scat}|_{Copper\,Plate}](dB) \tag{8}$$

$$\Delta\varphi = S_{11,scat}(\text{deg})|_V - S_{11,scat}(\text{deg})|_{V=0\text{V}}. \tag{9}$$

The voltage steering process starts from 0 to 36.0 V with steps of 0.2 V and scattered field is measured. The measured amplitudes and phases [see (9)] of scattered field at different bias voltages are shown in Fig. 9(b); when the LC RA is biased with 0 V, magnitude of reflected wave is −6.8 dB, with bias voltage increasing to 6.0 V where there is no change; when the bias voltage is higher than 6.0 V, the magnitude started to change. It gets lower first and then gets higher with increasing voltage, but at the bias voltage from 7.0 to 10.0 V, there is a cave, which may be caused by the resonance. The steered tendency of reflected phase also started to change at 6.0 V; compared with magnitude, the phase changes relatively monotonously, the phase gets lower, and phase difference can reach −338° when bias voltage reaches 36.0 V. Even though the phase-varying ability cannot reach 360° within bias voltage of 0–36.0 V, approximation in phase compensation works for the beam steering.

Reference to a copper plate of the same size, our LC RA design exhibits a change in reflected wave magnitude from −6.8 to −10.2 dB as the bias voltage increases from 0 to 36 V, corresponding efficiency varies from 22.9% to 15.5%. Table II presents the reconfigurable reflection coefficients of published LC RAs. In comparison to these LC RA designs, our proposed design demonstrates relatively small value in maximum loss in the reflected wave, with only a 3.4 dB difference between the highest and lowest reflected magnitude values. This small variation is advantageous for effective beam scanning. Furthermore, our design offers a controllable phase shift range of 338°, a value that ranks second only to the results reported in [38]. The comparison reveals that our design provides an LC RA unit that balances reflection magnitude and phase shift.

TABLE II
RECONFIGURABILITIES OF LC RA

Reference	Frequency	Min(|Γ|)	Δ|Γ| =|Γ|$_{MAX}$-|Γ|$_{MIN}$	Phase shift
[23]	78 GHz	-17 dB	7 dB	270°
[24]	35 GHz	-11 dB	10 dB	250°
[38]	104.2 GHz	-20 dB	20 dB	350.7°
[39]	77 GHz	-22.5 dB	22.5 dB	280°
[26]	9.55 GHz	-2.3 dB	2.2 dB	260°
This work	37.5 GHz	-10.2 dB	3.4 dB	338°

IV. BEAM STEERING RESULTS

Since the reconfigurable LC RA is a system which consists of the feed antenna, LC RA, bias lines, voltage output modules, and computer, it needs all parts to cooperate properly to achieve steerable beam to the target direction. When the

LC RA is manufactured, placement of the feed antenna, values of bias voltage, and measurement scheme should be taken into account. And we design our LC RA system as shown in Fig. 1(a) considering the relationship of position and controlling model.

A. Position of Feed Antenna

How to locate the feed antenna upon RA should be considered carefully because the geometrical placement influences a lot on the system performance. Large F/D brings high illumination efficiency but also cause high edge taper which results in low spillover efficiency; small F/D increases the spillover efficiency and lower the edge taper of RA which can guarantee that incident wave is mostly utilized to steer beam although the illumination efficiency declines. Since the total aperture efficiency equals the product of spillover efficiency and illumination efficiency, it is a tradeoff to select F when considering the maximum utilization of RA [31]. The RA antenna system usually chooses an offset placement of the feed antenna to avoid feed blockage when the system is controlled to scan beam, which can lower the physical occlusion effect of feed antenna, meanwhile oblique incidence from feed to RA appears, so the oblique incident reflection response should be studied before final decision.

In most published RA systems, the RA is usually placed in the near-field region of the feed [32] where high gain feed antenna causes high illumination efficiency, but the incident field on elements cannot be considered as plane-wave seriously. Without regarding the proposed LC RA system, the far-field region of feed antenna is off the center with a diameter more than 324.0 mm, namely, $F/D = 6.48$ is required to satisfy the far-field radiation condition of the feed in the RA system, where the spatial phase delay of the RA element is proportional to the distance form phase center of feed to the element, but the edge taper will influence the pattern of the RA. In this study, a standard horn antenna of 20 dBi at Ka band is used as feed, and the reconfigurable LC RA has an aperture size of 50.0 × 50.0 mm ($6.25\lambda \times 6.25\lambda$). In this condition, if we put the RA at the far-field of the feed, the edge taper of the RA aperture is −0.7 dB by approximate calculation with cosine q pattern, which causes obvious loss of power and efficiency; besides, the influence of the corner and edge of the RA will also cause the reflected beam worse. A near-field region distance of 140.0 mm from the flange of the horn antenna to the RA surface is selected, as the phase center of the antenna is 60.0 mm from the flange, with an offset angle 20°; thus $F/D = 1.67$. To find the incident wave on the RA surface more accurately, MoM is used to calculate the incident near-field distribute on the RA element, which is shown in Fig. 10. The magnitude of co-polarized incident wave |Ex| is plot in Fig. 10(a), edge taper is around −7.5 dB, a relatively low level, the magnitude of cross-polarized incident wave |Ey| is plot in Fig. 10(b); compared with |Ex|, the values are smaller and the cross polarized wave influences a little to the RA; the phase of Ex and Ey is plot in Fig. 10(c) and (d) and these values have relationship with feed antenna and Euclidean distance and coupling.

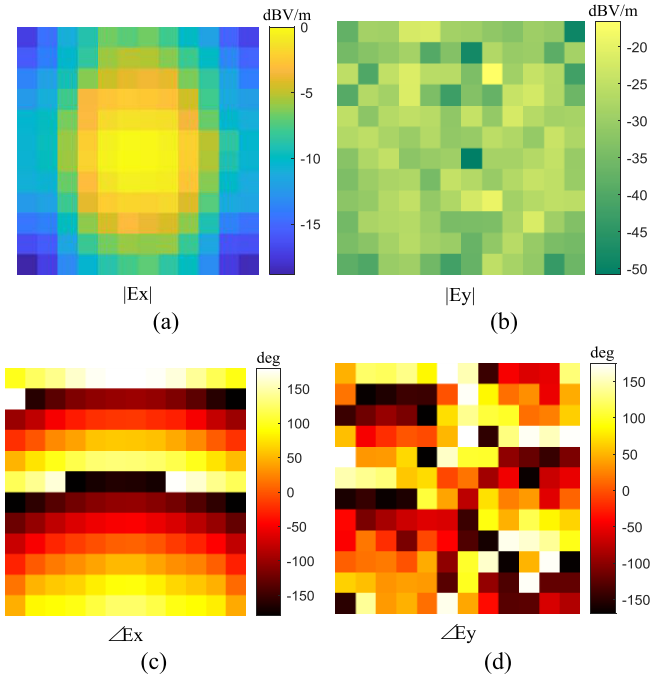

Fig. 10. Field components of incident field from feed antenna on the LC RA surface. (a) Magnitude of co-polarization field. (b) Magnitude of x-polarization field. (c) Phase of co-polarization field. (d) Phase of x-polarization field.

B. Controlling Scheme

The phase compensation scheme-steering beam and reflected wave from RA unit should compensate the space phase on the RA surface in Fig. 10(c) since |Ex| is much larger than |Ey|. When the phase compensation scheme is applied to the reconfigurable RA, each element is controlled to achieve steered phase according to the desired direction $\hat{k}_{\mathbf{0}}$; the phase compensation ability of reconfigurable RA converts the incident quasi-spherical wave radiated by the feed antenna, to a collimated beam in the direction $\hat{r}_{\mathbf{0}}$, and the phase of reflected wave on RA aperture is approximately planar and progressive phase distribution $\phi_{\mathbf{pp}}$

$$\varphi_{pp} = -k_0 \hat{r}_0 \cdot \vec{r}_{mn} \tag{10}$$

where k_0 is free space wavenumber, m and n are the order of the RA elements along directions x and y, $\hat{r}_{\mathbf{0}}$ is the unit vector of the direction that EM wave, $\vec{r}_{\mathbf{mn}}$ is the coordinate vector that form the origin to the mnth element of RA, m represents the column order in the RA, and n represents the row order in the RA. The propagation direction vector of EM wave $\hat{r}_{\mathbf{0}}$ can be expressed in a certain direction expressed in spherical coordinate θ_o, φ_o, to get a beam directed in a certain spherical direction (θ_o, φ_o) relative to axis z, the mnth element with a coordinate (x_{mn}, y_{mn}) should have a progressive phase, so the progressive phase distribution ϕ_{pp} can be written in another expression

$$\varphi_{pp,mn} = -k_0(x_{mn}\sin\theta_0\cos\phi_0 + y_{mn}\sin\theta_0\sin\phi_0) \tag{11}$$

$$\varphi_{RA,mn} = \varphi_{pp,mn} - \varphi_{Near\_Ex,mn} + \varphi_0. \tag{12}$$

Here ϕ_{pp_mn} is the compensation phase of the mnth RA element to form a beam pointing at the direction $\hat{r}_{\mathbf{0}}$, and ϕ_0 is a referenced phase constant, indicating a relative phase is

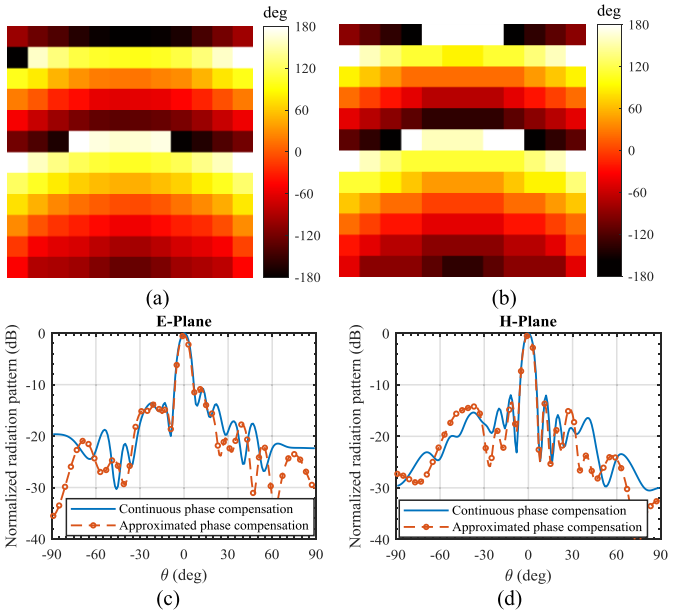

Fig. 11. Calculated results of steered beam at far-field. (a) Continuous phase compensation for RA. (b) Approximation phase compensation for RA. (c) H-plane. (d) E-plane.

needed for RA elements. The RA element should be biased with a certain voltage value which can steer the LC unit with a state that equals the phase $\phi_{pp,mn}$, and the relationship can be obtained from Fig. 9(b). The biased relationship between the compensation phase of the mnth element and the mnth bias voltage connection line is

$$\varphi_{RA,mn} = f[g(V_{mn})]. \tag{13}$$

Sometimes the reflection phase of the RA unit is needed to reach the phase tuning ability over the maximum phase of our 2-finger structure which has 338°, so the required phase from −338° to −349° can be approximated to −338°, approximation 0° can be applied from −349° to −360°, such an error may influence the beam a little. Here the approximation reflection phase is $\angle\Gamma_{xx,mn}$, since in the RA system, the co-polarization of the antenna and the polarization response of RA unit in the coordinate of the proposed RA system are all x-polarized.

To compensate phase of LC RA in Section IV-A to achieve beam pointing at $\varphi_o = 0°$, $\theta_o = 0°$, the required phase response of the RA to achieve this beam pointing is shown in Fig. 11(a), which ranges from −180° to 180°. The achieved phase controlled in our LC RA has a maximum phase variation of 388°, and it is added with a referenced phase ϕ_0 to achieve the desired phase response as shown in Fig. 11(b). After the phase compensation, the radiation pattern of the LC RA is evaluated in the E-plane [see Fig. 11(c)] and H-plane [see Fig. 11(d)]. The results show that the maximum radiation power of the approximated phase compensation is 0.4 dB lower than the continuous phase compensation. Additionally, the first SLL of the two compensation schemes has a difference of 0.5 dB in the E-plane and 1.1 dB in the H-plane. However, overall, a good agreement within 1.5 dB error is achieved in the range of ±20° at the maximum radiation. This phase compensation scheme allows the LC RA to precisely steer the beam to the desired direction, achieving accurate beam pointing and radiation performance in both the E-plane and H-plane, making it suitable for practical applications in reconfigurable RA systems.

C. Steering Beam at E-Plane and H-Plane

The steered beams of the LC RA antenna have been measured in experiment for several scan angles at target frequency of 37.5 GHz. For the scanning plane of H-plane and E-plane, a far-field radiation pattern measurement system is built: the standard horn antenna at Ka band is chosen as the receiving antenna, the LC RA is placed at the center of rotating axis of the optic turn table, the 20 dBi standard horn antenna is placed 20° offset at the place where the flange of antenna is 140.0 mm from the RA along direction z and it is connected to the bias lines from the pin points to the amplifier which can output magnified voltage from voltage controller. If a beam toward a certain direction is needed, codes from PC can control the voltage controller, then ac of low frequency can be added to the LC RA element, the phase of reflected wave changes, and the beam will change. The RA and antenna are surrounded by radio absorber. The measuring schemes are shown in Fig. 12.

If we choose the coordinate system same as Fig. 12(a), the origin locates at the center of RA center, the axis $+z$ is along the normal direction of the RA upper surface, axis x is along the dipole of the RA unit, and axis y is parallel to the patch bias line of the patch layer. Since the feed antenna is placed with an incident angle $\theta_o = 20°$, the maximum radiation is $\theta = 20°$, $\varphi = 90°$. According to the definition, H-plane is the yOz plane [see Fig. 12(a)], E-plane is the xOz' plane (Fig. 12(b), and z' is the axis z rotate around x). The measured results of steered beam toward $\theta_o = 0°$, 10°, 20°, 30°, and 40° at H-plane are compared in Fig. 13(a), from where we can see that the maximum radiation pattern in H-plane is toward 20° with a SLL of −10.2 dB, when the beam scans to broadside or endfire gain decreases; at $\theta_o = 40°$, gain decreased to −3.5 dB, SLL increased to −7.9 dB; when beam scanned to $\theta_o = 0°$, gain reduced to −3.2 dB, SLL reached to −6.1 dB. The steered beam toward $\theta_o = 0°$, 10°, 20°, and 35° at E-plane are plot in Fig. 13(b) and the maximum radiation pattern of steered beam is at $\theta_o = 0°$, with a SLL of −14.0 dB; when the angle started to increase, the gain declined and SLL increased, when it reaches to $\theta_o = 35°$, the gain decreased to −3.7 dB, SLL varied to −8.3 dB.

Compared with steered beams at E-plane, the beams at H-plane have relatively higher SLLs; this is caused by the position of feed antenna which is located at H-plane and has an angle shifted relative to the normal direction; thus, the steered beam at H-plane had poor beam. According to the discussion with other scholars, we all think that the feed antennas in the RA antenna system will cause physical obstacles; thus, the choice of a proper antenna and placement relationship will optimize the pattern to some degree.

D. Any Direction at 2-D Space

Since the LC RA system use offset feed can reduce the obstacle to some degree, but when measure the pattern of the

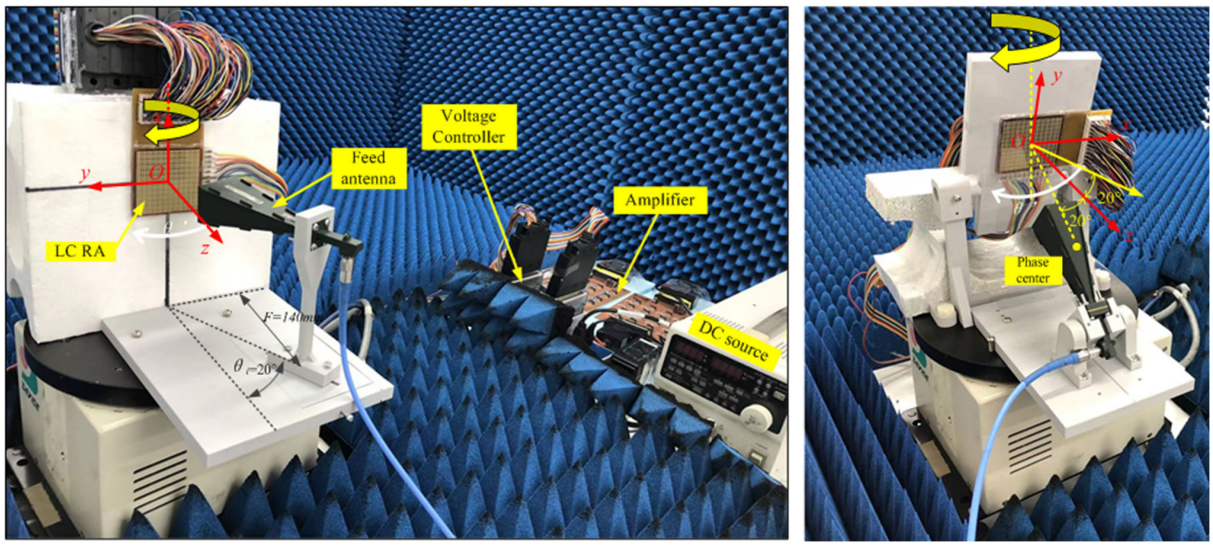

Fig. 12. Experimental scene of the steered beam at far-field. (a) H-plane. (b) E-plane.

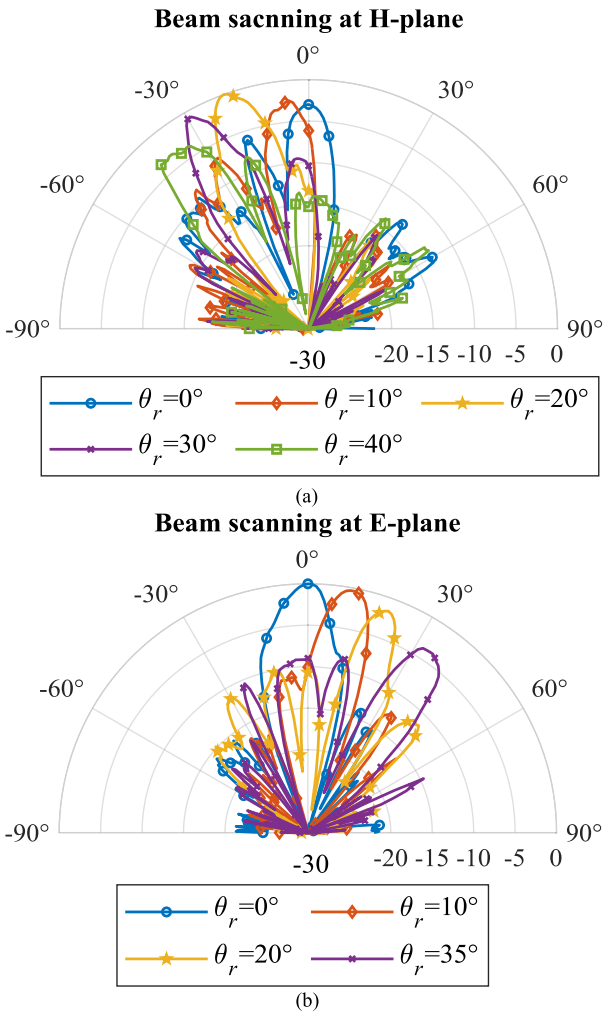

Fig. 13. Measured results of steered beam at far-field. (a) H-plane. (b) E-plane.

LC RA system steered at a particular direction, new fixtures to locate the feed antenna and RA are required, and we shall make sure that the maximum radiation direction is in the horizontal plane of turn table during rotation, thus a lot of machinal work shall be done. To measure the steered beam toward a particular direction which is not located in H-plane or E-plane, a near-field measurement system was constructed [illustrates in Fig. 14(a)], the position details are shown in Fig. 14(b), LC RA is placed at defined center of the tested scene, the feed antenna is placed in front of the RA with a distance of 140.0 mm (from flange of the antenna to the RA surface) and an incident angle of $\theta_f = 20°$, polarization is along direction x.

To measure the far-field radiation pattern of LC RA in the near-field region, it is necessary to collect the near-field distribution, the schematic of near-field data acquisition for the RA is shown in Fig. 14(b), the probe is placed with 180.0 mm from the RA, and the probe measure the co-polarization and x-polarization field in an area of 500.0 × 500.0 mm with a step of 4.0 mm ($\lambda_0/2$ @ $f = 37.5$ GHz). Once the reflected field $\vec{E}_\mathbf{r}$ on at the Fresnel region of the RA is known, planar near field to far-field transformation (mainly Fourier transform) can be applied to calculate the far-field $\vec{E}_\mathbf{T}$ of the RA

$$\begin{aligned}\vec{E}_T(x = ru, y = rv, z = rw) &= \frac{1}{4\pi^2}\int_{-\infty}^{\infty}\int_{-\infty}^{\infty} \times \left[\vec{F}_T(k_x, k_y, z = 0) - \hat{e}_z \frac{\vec{k}_T \cdot \vec{F}_T(k_x, k_y, z = 0)}{k_z}\right] \cdot e^{-j(k_x u + k_y v + k_z w)} dk_x dk_y \quad (14)\\ x &= r\sin\theta\cos\varphi = ru\\ y &= r\sin\theta\sin\varphi = rv\\ z &= r\cos\theta = rw. \quad (15)\end{aligned}$$

Here $\vec{F}_\mathbf{T}$ is the spectral component of the reflected near field of the RA

$$\vec{F}_T(k_x, k_y, z = 0) = \int_{-\infty}^{\infty}\int_{-\infty}^{\infty} \vec{E}_r(x, y, z = 0) e^{j(k_x x + k_y y)} dx dy. \quad (16)$$

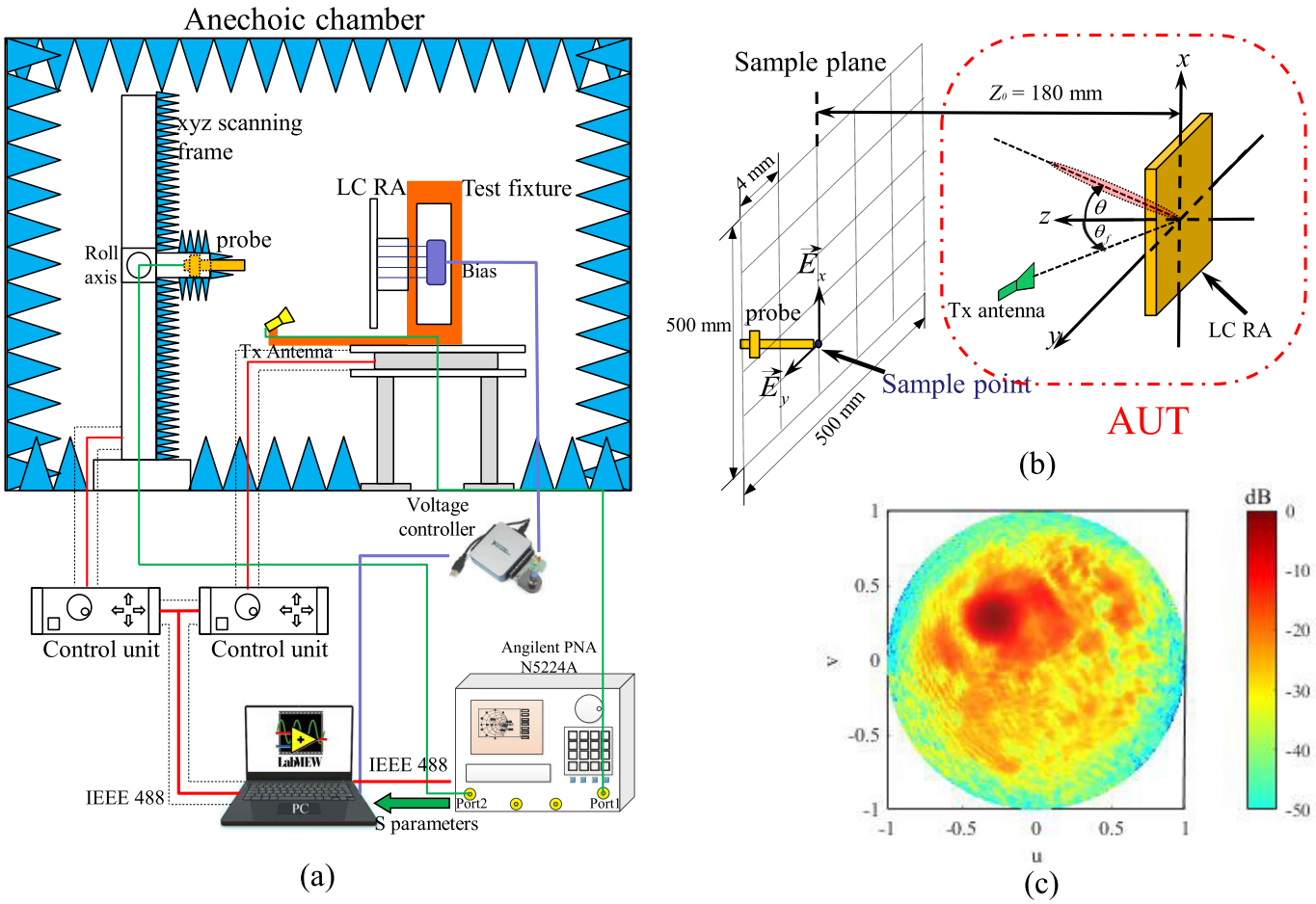

Fig. 14. Near-field measurement of LC RA system. (a) System description. (b) Sample points indication. (c) Radiation pattern.

And the wave far-field is traveling wave, so it should meet the physical properties when do Fourier transform

$$0 \le k_z = \sqrt{k_0^2 - k_x^2 - k_y^2} \le k_0 \tag{17}$$

$$\int_{-\infty}^{\infty}\int_{-\infty}^{\infty} \vec{E}_r(x, y, z = 0)e^{j(k_x x + k_y y)}dxdy < \infty. \tag{18}$$

When reflected wave at far-field is calculated, the normalized directivity can be computed by definition; this can be seen in the radiation pattern expressed in UV shown in Fig. 14(c), which exhibit the 3-D beam and plane pattern at a direction that does not locate E-plane or H-plane, for example, $\varphi_a = 115°$, $\theta_a = 15°$.

E. Response Time of LC RA

As the response time of RIS is an important performance, especially at the application scene when the end users are moving. Related experiment of evaluating the response time of LC RA is shown in Fig. 15. According to the H-plane radiation pattern measurement results in Section IV-C, proper bias voltage is added to the LC RA using the reconfigurable system. When the beam is controlled toward a certain direction ($\theta_r = 0°$, 10°, 20°, 30°, and 40°), the S parameter at the delay time T is collected by the VNA. If the S parameter at time T is within 5% error tolerance, the response time T of beam pointing at θ_r is measured. As the rise time and fall time of

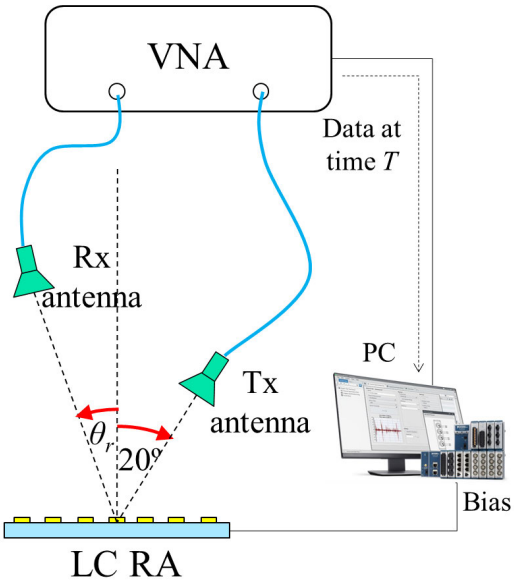

Fig. 15. Schematic of measuring response time for LC RA at several directions.

LC under the electrodes are different, the response times of LC RA when turn on and turn off are divergent. The response time measurement of LC RA is shown in Table III, the term Ton represents the reaction time when LC RA is biased with relative voltage, Toff is the response time when the bias voltage

TABLE III
RESPONSE TIME OF LC RA

Beam direction	0°	10°	20°	30°	40°
Ton (s)	0.95	1.05	0.96	1.03	1.08
Toff (s)	5.75	6.05	5.955	5.87	6.15

is turned off. Form the table, the Ton time toward the directions $\theta_r = 0°$, 10°, 20°, 30°, and 40° are 0.95, 1.05, 0.96, 1.03, and 1.08 s. In the similar way, the time of LC RA from bias state to without bias are measured, the time Toff of five directions are 5.75, 6.05, 5.955, 5.87, and 6.15 s. Therefore, the average time of switching beam is approximately 1 s, the average response time of shutting down beam is nearly 6 s.

From the point of the response time switching beam, LC RA does not have obvious advantages over other technologies in the future wireless communication system which needs fast beam switch (such as millisecond [3]), since RIS needs fast reaction time to point at end users to cover the spot areas. Therefore, increasing the reaction speed is a hot research topic for LC RA in communication. It is worthwhile to mention that the response time can be further reduced by some technologies borrowed from optic industries (such as the overdrive bias scheme [19]), thus the response time of LC RA can be reduced to millisecond range.

V. APPLICATION OF LC RA AS RIS

In practical application of RIS, it is often placed on the surface of tall buildings to control the direction of incident electromagnetic waves and direct scattering wave to specific areas that may be uncovered. In our LC RA system, we assume that a plane wave is incident from the direction of $\varphi = 0°$, $\theta = 8°$ onto the surface of the LC RA. By controlling the LC RA unit and adjusting the phase of the reflected wave, we can manipulate the direction of the scattered wave to $\varphi = 0°$, $\theta = 0°$. In the context of low-bit phase quantization schemes, quantization lobes can be a problem in RIS applications [33]. However, our proposed LC RA system is capable of continuous phase compensation and has a large phase shift range, effectively avoiding this issue. Fig. 16 illustrates calculated scattering patterns of four different phase compensation schemes: 1-bit quantization, 2-bit quantization, LC RA with continuous phase compensation, and LC RA with phase compensation + random phase optimization.

From Fig. 16, we observe that the 1-bit quantization scheme exhibits two symmetric main beams, while the 2-bit quantization scheme only has one main beam pointing exactly to $\varphi = 0°$, $\theta = 0°$, with a SLL of -8.1 dB. On the other hand, the LC RA with continuous phase compensation enables the scattered beams to point accurately to $\varphi = 0°$, $\theta = 0°$, with an SLL of only -11.2 dB. By further adding a random phase φ_0 through the optimization process described in (12), the SLL can be further reduced to -13.9 dB. Therefore, our proposed LC RA system, with its all-phase compensation and random phase optimization, effectively reduces the SLL compared to low-bit quantization schemes, making it a promising solution for RIS applications to achieve precise and efficient beam steering.

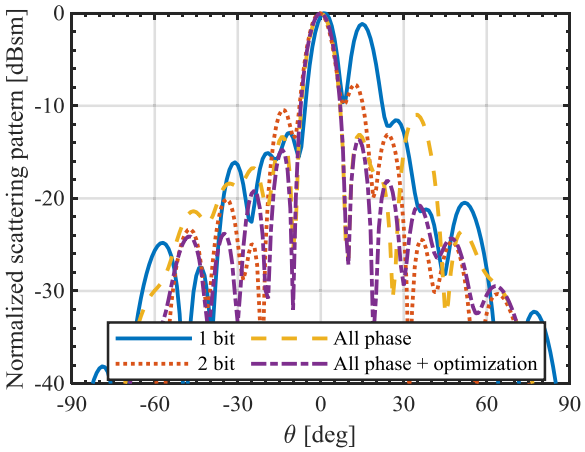

Fig. 16. Scattering pattern of LC RA with different phase compensation.

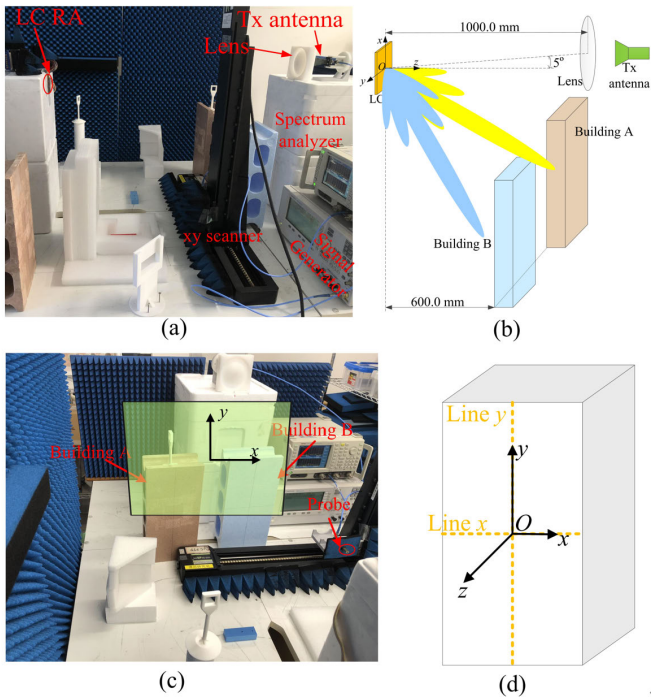

Fig. 17. Experiments for RIS application. (a) Experiment scene of application of LC RA as RIS. (b) Schematic of steered field to blind areas. (c) Steered beam to building A and B. (d) Measured routine on building A and B.

To imitate a realistic urban environment, a modern and highly developed urban area was constructed with models as shown in Fig. 17(a), with plastic models representing tall buildings to imitate a crowded environment. The base station antennas were found to be unable to reach the back of some buildings [building A and B shown in Fig. 17(c)], creating blind spots in coverage. In outdoor electromagnetic wave transmission scenarios, brick pillars and tinted glass, commonly found in building structures, can cause considerable loss of electromagnetic waves in the Ka band, with reported losses ranging from 20 to 30 dB [36]. The reflection of electromagnetic waves is mainly determined by the dielectric constant, also known as relative permittivity, of the medium. Glass typically has a relative permittivity ranging from 2.2 to 7.0, while the plastic materials used in the construction of the scene have relative permittivity values ranging from 2.2 to 4.4. Due to the differences in relative permittivity between glass

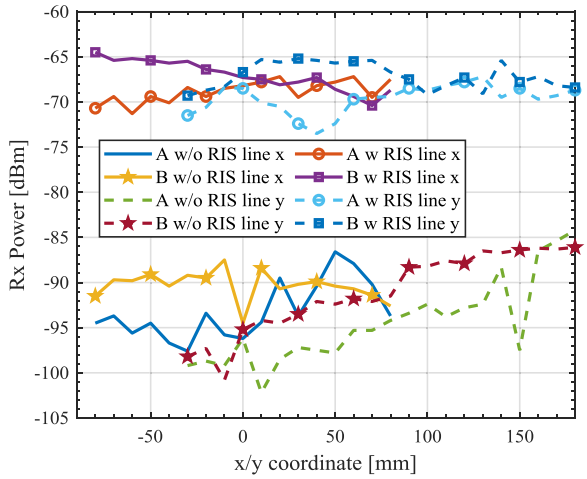

Fig. 18. Compare the received power at the condition of the scene with RIS and without RIS.

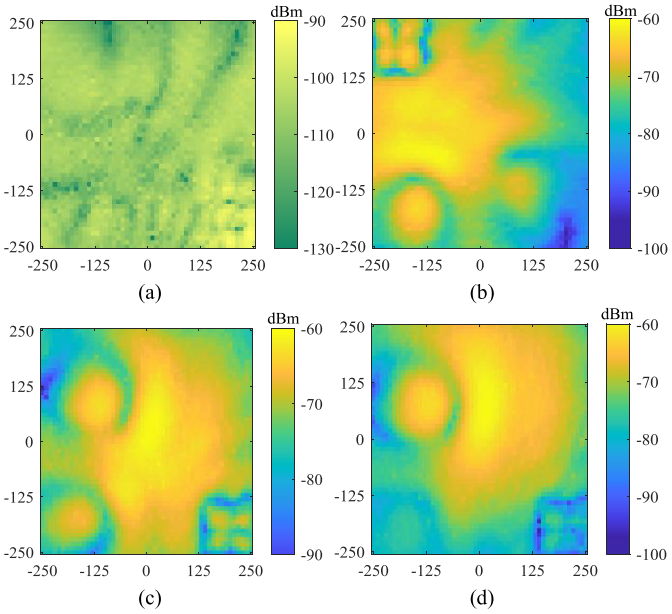

Fig. 19. Comparison of field distribution in front of building models with and without steering beams from RIS. (a) Field distribution w/o RIS. Field distribution when steer beam toward (b) $\theta = -15°$, (c) $\theta = 0°$, and (d) $\theta = 10°$.

and plastic, using a model built with plastic materials can provide a simulation of the crowded urban electromagnetic environment to a certain extent. To address this issue, RIS is researched to be added to extend the coverage area of the base station. By responding to user demand, the RIS can form a directional beam toward users in the shadow area, effectively covering the blind spots [see Fig. 17(b)].

In the simulated practical experiment, a lens is placed in front of a 20 dBi Ka band horn antenna to transverse the spherical wave to plane wave, which is practical and agrees well with the practical case. The addition of this lens enhances the intensity of the wave incident on the RIS surface and increase signal noise ratio. The LC RA is placed about 1.0 m from the transmit antenna (Tx antenna) with angle of 5° to the normal direction of Tx antenna, two buildings A and B are placed between Tx and LC RA and they are set about 600.0 mm from the LC RA whose far-field range is larger than 324.0 mm, the center of the buildings have angles of $\varphi_A = 206°$, $\theta_A = 35.1°$ and $\varphi_B = 180°$, $\theta_B = 34.3°$ relative to the center of RA, apply proper voltages to the RA by the controlling scheme expressed in Section IV-B, the waves can be transmitted to the building A and B, but the phase $\varphi_{Near\_Ex,mn}$ is replaced with a constant since the waves coming from the feed can be approximated to plane wave. A xy scanner with absorber surrounding the device is used to measure the receiving power before the building A and B with receiving (Rx) antenna.

The measured routine is shown in Fig. 17(d), the center is the coordinate of the buildings, and measured Rx power is along the x line and y line marked in the figure with a step of 10.0 mm, in which measured results of Rx power without and with RIS are compared in Fig. 18. To the building A, the application of LC RA increased the receiving power by 18.8–29.2 dB compared the condition without LC RA during the procedure when Rx antenna moving along line x, while increased 15.5–32.1 dB along line y. For building B, the addition of LC RA improves the received energy by 20.8–27.2 dB in the line x and 17.4–32.5 dB in the line y, respectively, compared to the absence of RA as an intermediary. These comparative experiments show that the programable LC RA can act as a relay to direct the scattered wave to the blind areas of the base station antenna and enhance the received signal strength.

In our subsequent experiments, we focused on evaluating the 2-D electric field distribution at 37.5 GHz under two scenarios: one without the presence of a RIS and the other with RIS-controlled beam scanning. The experimental setup involved a scanning area represented as a square bordered by an xy scanner, with dimensions of 500 × 500 mm. The coordinate origin was established as a point located 250 mm above the ground at the midpoint between two building models A and B. This experiment consists of measuring three coverage scenes: building A, middle between buildings A and B, and building B. The corresponding scanning angles are −15°, 0°, and 10°, respectively. The covering area is shown in Fig. 17(c) plot with transparent green color and probe moves in this area to measure the receiving power. When there was no RIS in place, the received power distribution in front of the buildings was captured, as shown in Fig. 19(a). The received power ranged from −130 to −90 dBm, illustrating the varying signal strengths across the scanning area. Subsequently, when the LC RA was employed as the RIS and beam scanning was initiated in the horizontal plane (H-plane), distinct scanning angles were chosen. Specifically, the beams were steered to −15°, 0°, and 10°, as presented in Fig. 19(b)–(d), respectively. Upon analysis, it was observed that the power of the EM waves in front of the building models was significantly boosted when the beam was steered to the specified angles. The received power exhibited a notable increase, ranging from −100 to −60 dBm. This enhancement is quite significant, as it effectively overcomes the influence of surrounding obstacles and contributes to covering the blind areas of EM wave coverage. This enhancement remains effective even in the

TABLE IV
PERFORMANCE COMPARISON OF LC RA

Reference	Frequency	Polar.	No. of layers	Phase shift	SLL	Scanning capability	Scanning range	Reaction time	Application as RIS	Power increased
[23]	78 GHz	Linear	3	305^0	-6 dB	1-D	12^0	-	-	-
[24]	35 GHz	Linear	3	250^0	-4 dB	1-D	20^0	-	-	-
[22]	102 GHz	Linear	3	330^0	-13 dB	1-D	55^0	2 s	-	-
[39]	77 GHz	Linear	3	280^0	-8 dB	1-D	25^0	-	-	-
[26]	9.55 GHz	Linear	4	260^0	-15.4 dB	2-D	50^0	-	-	-
This work	37.5 GHz	Linear	3	338^0	-14 dB	2-D	35^0	t_{on}: 1.05 s t_{off}: 6.05 s	Yes	$\geqslant$ 18.8 dB

presence of various obstacles, making it a promising approach to mitigate blind spots in EM wave coverage.

We compare the performance of our proposed LC RA with published works in Table IV. Our proposed design has a relative larger phase shift range 338° than other works, the large phase shift will benefit the beam forming, scanning capabilities, and beam optimization. For the SLL, we have relative good beam shape compared with a small value of −14 dB, even though there is better performance in [26]. In terms of its beam scanning capabilities, by integrating solid metallic vias and the corresponding bias circuits for LC RA, we achieve 2-D beam scanning, which represents a notable advancement over the capabilities of most LC RAs. Furthermore, in comparison to the methodology presented in [26], we use fewer layers, which can effectively reduce the cost. Moreover, we measure the response time of LC RA scanning in all directions, and the beam change time is less than 1.05 s, which makes this antenna usable for many applications. Additionally, we have explored the utilization of the LC RA as a RIS to eliminate blind spots in electromagnetic wave coverage. Remarkably, our RIS implementation has demonstrated an enhancement of over 18.8 dB in the received signal strength, underscoring the potential impact of our approach in improving communication quality and coverage.

VI. CONCLUSION

In this article, a LC RA unit with separate ground and bias point is proposed based on the studies of previous scholars, this updated unit and the metalized vias network working together can achieve reflection coefficient steerable at two dimensions, so each LC RA unit can be controlled individually according to demands. At target frequency $f = 37.5$ GHz, the proposed RA unit can achieve phase shift around 360° and high polarization response with oblique incident condition at a relative wide angle from 0° to 45°. Then a 12 × 12 element LC RA is manufactured, checked reconfigurability, and measured the steered phase by voltage, a phase variation of 338° is achieved by the measurement.

We chose the Ka band standard horn antenna offset 20° at H-plane as the feed, and the incident field on the surface of RA with element space of $\lambda_0/2$ calculated by MoM. The steered beam by voltage at both H-plane and E-plane are measured at far-field region, beam scanning at H-plane can cover 0°–40° when the maximum radiation direction is at 20°, when the beam is steered to 0°, gain lost 3.2 dB and the SLL increased to −6.1 dB, as the measured beam pointing to 40°, the gain decreased 3.5 dB, SLL reached −7.9 dB; E-plane scanning is measured from 0° to 35°, the gain declined 3.7 dB, and SLL rose to −8.3 dB; to measure the special direction beam (pointing to $\varphi_a = 115°$, $\theta_a = 15°$), a near-field measurement is constructed, and it showed the proposed LC RA can achieve the beam steering at two dimensions. Then LC RA was used as a RIS to improve the receiving signal strength and compensate for the blind spot of two simulated EM wave blind areas in a crowded neighborhood street model.

In future work, we would like to develop magnitude analysis and SLL depression synthesis. This will help us to design a RA with higher total efficiency and a higher gain with lower SLL even scan to large angles, and we honestly hope it could be a contribution to the application of RIS in the future.

ACKNOWLEDGMENT

The authors are grateful to Prof. Sawaya for the guidance and knowledge of electromagnetic and antenna, besides, they would like to acknowledge the assistance of Mr. Fujisawa.

REFERENCES

[1] E. Basar, M. Di Renzo, J. De Rosny, M. Debbah, M.-S. Alouini, and R. Zhang, "Wireless communications through reconfigurable intelligent surfaces," *IEEE Access*, vol. 7, pp. 116753–116773, 2019.

[2] A. Shojaeifard et al., "MIMO evolution beyond 5G through reconfigurable intelligent surfaces and fluid antenna systems," *Proc. IEEE*, vol. 110, no. 9, pp. 1244–1265, Sep. 2022.

[3] F. Shu, G. Yang, and Y.-C. Liang, "Reconfigurable intelligent surface enhanced symbiotic radio over multicasting signals," in *Proc. IEEE 93rd Veh. Technol. Conf. (VTC-Spring)*, Apr. 2021, pp. 1–6.

[4] N. S. Perovic, L.-N. Tran, M. Di Renzo, and M. F. Flanagan, "Achievable rate optimization for MIMO systems with reconfigurable intelligent surfaces," *IEEE Trans. Wireless Commun.*, vol. 20, no. 6, pp. 3865–3882, Jun. 2021.

[5] C. Pan et al., "Reconfigurable intelligent surfaces for 6G systems: Principles, applications, and research directions," *IEEE Commun. Mag.*, vol. 59, no. 6, pp. 14–20, Jun. 2021.

[6] X. Cao, Q. Chen, T. Tanaka, M. Kozai, and H. Minami, "A 1-bit time-modulated reflectarray for reconfigurable-intelligent-surface applications," *IEEE Trans. Antennas Propag.*, vol. 71, no. 3, pp. 2396–2408, Mar. 2023.

[7] G. C. Alexandropoulos and E. Vlachos, "A hardware architecture for reconfigurable intelligent surfaces with minimal active elements for explicit channel estimation," in *Proc. IEEE Int. Conf. Acoust., Speech Signal Process. (ICASSP)*, May 2020, pp. 9175–9179.

[8] J. A. Hodge, K. Vijay Mishra, Q. M. Nguyen, and Amir. I. Zaghloul, "Generalized polarization-space modulation in reconfigurable intelligent surfaces," in *Proc. 54th Asilomar Conf. Signals, Syst., Comput.*, Pacific Grove, CA, USA, Nov. 2020, pp. 712–717.

[9] K. Xu and J. H. Choi, "Liquid-metal-tuned patch element for flexible and reconfigurable reflectarrays/intelligent surfaces," in *Proc. IEEE Int. Symp. Antennas Propag. USNC-URSI Radio Sci. Meeting (APS/URSI)*, Dec. 2021, pp. 79–80.

[10] R. L. Haupt and M. Lanagan, "Reconfigurable antennas," *IEEE Antennas Propag. Mag.*, vol. 55, no. 1, pp. 49–61, Feb. 2013.

[11] X. Tan, Z. Sun, J. M. Jornet, and D. Pados, "Increasing indoor spectrum sharing capacity using smart reflect-array," in *Proc. IEEE Int. Conf. Commun. (ICC)*, Kuala Lumpur, Malaysia, May 2016, pp. 1–6.

[12] P. Nayeri, F. Yang, and A. Z. Elsherbeni, "Beam-scanning reflectarray antennas: A technical overview and state of the art," *IEEE Antennas Propag. Mag.*, vol. 57, no. 4, pp. 32–47, Aug. 2015.

[13] W. Wu, K.-D. Xu, Q. Chen, T. Tanaka, M. Kozai, and H. Minami, "A wideband reflectarray based on single-layer magneto-electric dipole elements with 1-bit switching mode," *IEEE Trans. Antennas Propag.*, vol. 70, no. 12, pp. 12346–12351, Dec. 2022.

[14] M. Wang, S. Xu, F. Yang, and M. Li, "A 1-bit bidirectional reconfigurable transmit-reflect-array using a single-layer slot element with PIN diodes," *IEEE Trans. Antennas Propag.*, vol. 67, no. 9, pp. 6205–6210, Sep. 2019.

[15] F. Wu, R. Lu, J. Wang, Z. H. Jiang, W. Hong, and K.-M. Luk, "A circularly polarized 1 bit electronically reconfigurable reflectarray based on electromagnetic element rotation," *IEEE Trans. Antennas Propag.*, vol. 69, no. 9, pp. 5585–5595, Sep. 2021.

[16] O. Bayraktar, O. A. Civi, and T. Akin, "Beam switching reflectarray monolithically integrated with RF MEMS switches," *IEEE Trans. Antennas Propag.*, vol. 60, no. 2, pp. 854–862, Feb. 2012.

[17] J. Huang and R. J. Pogorzelski, "A Ka-band microstrip reflectarray with elements having variable rotation angles," *IEEE Trans. Antennas Propag.*, vol. 46, no. 5, pp. 650–656, May 1998.

[18] S. V. Hum, G. McFeetors, and M. Okoniewski, "Integrated MEMS reflectarray elements," in *Proc. 1st Eur. Conf. Antennas Propag.*, Nice, France, Nov. 2006, pp. 1–6.

[19] R. Guirado, G. Perez-Palomino, M. Ferreras, E. Carrasco, and M. Caño-García, "Dynamic modeling of liquid crystal-based metasurfaces and its application to reducing reconfigurability times," *IEEE Trans. Antennas Propag.*, vol. 70, no. 12, pp. 11847–11857, Dec. 2022.

[20] R. Guirado, G. Perez-Palomino, M. Caño-García, M. A. Geday, and E. Carrasco, "Mm-wave metasurface unit cells achieving millisecond response through polymer network liquid crystals," *IEEE Access*, vol. 10, pp. 127928–127938, 2022.

[21] M. Y. Ismail and R. Cahill, "Beam steering reflectarrays using liquid crystal substrate," in *Proc. High Freq. Postgraduate Student Colloq.*, Leeds, U.K., Sep. 2005, pp. 62–65.

[22] G. Perez-Palomino et al., "Design and demonstration of an electronically scanned reflectarray antenna at 100 GHz using multiresonant cells based on liquid crystals," *IEEE Trans. Antennas Propag.*, vol. 63, no. 8, pp. 3722–3727, Aug. 2015.

[23] S. Bildik, S. Dieter, C. Fritzsch, W. Menzel, and R. Jakoby, "Reconfigurable folded reflectarray antenna based upon liquid crystal technology," *IEEE Trans. Antennas Propag.*, vol. 63, no. 1, pp. 122–132, Jan. 2015.

[24] A. Moessinger et al., "Electronically reconfigurable reflectarrays with nematic liquid crystals," *Electron. Lett.*, vol. 42, no. 16, pp. 899–900, Aug. 2006.

[25] J. X. Li et al., "Design and numerical demonstration of a 2D millimeter-wave beam-scanning reflectarray based on liquid crystals and a static driving technique," *J. Phys. D, Appl. Phys.*, vol. 52, no. 27, 2019, Art. no. 275103.

[26] H. Kim, J. Kim, and J. Oh, "Communication a novel systematic design of high-aperture-efficiency 2D beam-scanning liquid-crystal embedded reflectarray antenna for 6G FR3 and radar applications," *IEEE Trans. Antennas Propag.*, vol. 70, no. 11, pp. 11194–11198, Nov. 2022.

[27] X. Li, H. Sato, Y. Shibata, T. Ishinabe, H. Fujikake, and Q. Chen, "Development of beam steerable reflectarray with liquid crystal for both E-plane and H-plane," *IEEE Access*, vol. 10, pp. 26177–26185, 2022.

[28] S. Bulja, D. Mirshekar-Syahkal, R. James, S. E. Day, and F. A. Fernández, "Measurement of dielectric properties of nematic liquid crystals at millimeter wavelength," *IEEE Trans. Microw. Theory Techn.*, vol. 58, no. 12, pp. 3493–3501, Dec. 2010.

[29] P. Deo, D. Mirshekar-Syahkal, L. Seddon, S. E. Day, and F. A. Fernández, "Microstrip device for broadband (15–65 GHz) measurement of dielectric properties of nematic liquid crystals," *IEEE Trans. Microw. Theory Techn.*, vol. 63, no. 4, pp. 1388–1398, Apr. 2015.

[30] G. Perez-Palomino et al., "Accurate and efficient modeling to calculate the voltage dependence of liquid crystal-based reflectarray cells," *IEEE Trans. Antennas Propag.*, vol. 62, no. 5, pp. 2659–2668, May 2014.

[31] H. Yang et al., "A 1-Bit 10×10 reconfigurable reflectarray antenna: Design, optimization, and experiment," *IEEE Trans. Antennas Propag.*, vol. 64, no. 6, pp. 2246–2254, Jun. 2016.

[32] P. Nayeri, F. Yang, and A. Z. Elsherbeni, *Reflectarray Antennas: Theory Designs and Applications*. Hoboken, NJ, USA: Wiley, 2018.

[33] B. G. Kashyap, P. C. Theofanopoulos, and G. C. Trichopoulos, "Low sidelobe level randomized reconfigurable reflective surfaces under oblique incidence," in *Proc. United States Nat. Committee URSI Nat. Radio Sci. Meeting (USNC-URSI NRSM)*, Boulder, CO, USA, Jan. 2022, pp. 1–2.

[34] Y. Rong, P. C. Theofanopoulos, Y. Cui, G. C. Trichopoulos, and D. W. Bliss, "Non-contact reflectance based cardiac pulse detection from forehead, elbow and finger-tip using terahertz waves," in *Proc. IEEE Radar Conf. (RadarConf22)*, New York City, NY, USA, Mar. 2022, pp. 1–6.

[35] A. Sayanskiy et al., "A 2D-programmable and scalable reconfigurable intelligent surface remotely controlled via digital infrared code," *IEEE Trans. Antennas Propag.*, vol. 71, no. 1, pp. 570–580, Jan. 2023.

[36] T. S. Rappaport et al., "Wireless communications and applications above 100 GHz: Opportunities and challenges for 6G and beyond," *IEEE Access*, vol. 7, pp. 78729–78757, 2019.

[37] G. Perez-Palomino et al., "Design and experimental validation of liquid crystal-based reconfigurable reflectarray elements with improved bandwidth in F-band," *IEEE Trans. Antennas Propag.*, vol. 61, no. 4, pp. 1704–1713, Apr. 2013.

[38] S.-Y. Sun et al., "Electronically tunable liquid-crystal-based F-band phase shifter," *IEEE Access*, vol. 8, pp. 151065–151071, 2020.

[39] R. Marin, A. Moessinger, F. Goelden, S. Mueller, and R. Jakoby, "77 GHz reconfigurable reflectarray with nematic liquid crystal," in *Proc. 2nd Eur. Conf. Antennas Propag. (EuCAP)*, Edinburgh, U.K., Nov. 2007, pp. 1–5.

[40] H. Kim, S. Oh, S. Bang, H. Yang, B. Kim, and J. Oh, "Independently polarization manipulable liquid-crystal-based reflective metasurface for 5G reflectarray and reconfigurable intelligent surface," *IEEE Trans. Antennas Propag.*, vol. 71, no. 8, pp. 6606–6616, Aug. 2023.

Xiaotong Li (Student Member, IEEE) received the B.E. degree from the Agricultural University of Hebei, Baoding, China, in 2014, the M.E. degree from Xidian University, Xi'an, China, in 2017, and the D.E. degree from the Department of Communications Engineering, Tohoku University, Sendai, Japan, in 2023.

His current research interests include computational electromagnetic, method of moments, reflectarray antennas, reconfigurable antennas, and periodic structures.

Hiroyasu Sato (Member, IEEE) is currently an Assistant Professor with the Department of Communications Engineering, School of Engineering, Tohoku University, Sendai, Japan.

Hideo Fujikake (Senior Member, IEEE) is currently a Professor with the Department of Electronic Engineering, School of Engineering, Tohoku University, Sendai, Japan.

Qiang Chen (Senior Member, IEEE) is currently a Professor with the Department of Communications Engineering, School of Engineering, Tohoku University, Sendai, Japan.